SOILS AND FOUNDATIONS Vol. 39, No. 3, 37-52, June 1999
Japanese Geotechnical Society

FINITE ELEMENT MODELLING OF EXCAVATION AND ADVANCEMENT PROCESSES OF A SHIELD TUNNELLING MACHINE

KAZUHITO KOMIYA[i)], KENICHI SOGA[ii)], HIROKAZU AKAGI[iii)],
TOSHIYUKI HAGIWARA[iv)] and MALCOLM D. BOLTON[v)]

ABSTRACT

During shield tunnelling operation, a shield machine is driven forward by applying mechanical jack forces behind the machine tail and excavating the soil in front of the machine with its cutting face. In this study, the advancement and excavation processes of the shield tunnelling operation are modelled using the finite element method in order to investigate the effect of these construction processes on the ground response. A new excavating finite element, which models the disturbed soil in front of the cutting face, is introduced. The operation of shield advancement and of soil excavation is simulated using the finite element remeshing technique at each time step of the analysis. The accuracy of the finite element remeshing technique is discussed by analysing one-dimensional consolidation of an isotropic elastic medium. The proposed modelling techniques of shield tunnelling construction are applied to simulate a tunnelling project in Tokyo and the numerical results are compared with the field measurements. The soil deformation mechanism associated with the shield tunnelling operation is examined in detail.

Key words: cohesive soil, deformation, finite element method, stress, tunnel, water pressure (**IGC**: H5/E13)

INTRODUCTION

During shield tunnelling operations, the magnitude and distribution of the ground deformations are largely controlled by the construction process. The factors that affect the ground deformation are (Lee et al., 1992; Mair and Taylor, 1997):

(i) changes in earth pressure at the cutting face,
(ii) variation of external forces applied to the machine such as jacking forces,
(iii) shearing of soil at the shield-soil interface due to friction,
(iv) introduction of the tail void and injection of backfill between the tunnel lining and excavated tunnel cavity,
(v) overexcavation due to steering of the machine, and
(vi) long term consolidation due to excess pore pressure dissipation and changes in groundwater hydraulic conditions.

Many of the above factors are closely linked to the interaction between the soil and shield machine, which cause the stress state of the soil to change. The possible earth pressure changes due to the shield machine advancement are illustrated in Fig. 1. The figure is based on extensive earth pressure and deformation measurements of a sewer tunnel construction through soft ground in Tokyo conducted by Hashimoto (1984). The figure implies that the nature of the problem is three-dimensional and that the magnitude of earth pressure change is related to the machine characteristics, construction procedure, operator's control, etc. Therefore, when estimating the ground deformation caused by shield tunnel construction, care should be taken of how to model the character-

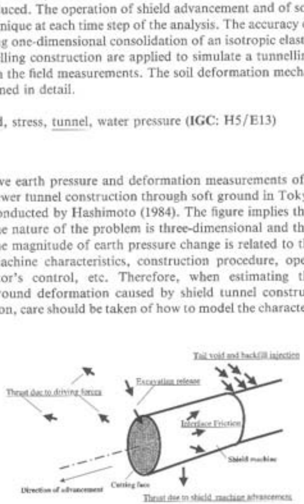

Fig. 1. Earth pressure changes due to the shield machine advancement (after Hashimoto, 1984)

[i)] Associate Professor of Civil Engineering, Chiba Institute of Technology, Japan and Research Associate in Engineering, University of Cambridge, UK.
[ii)] Lecturer in Engineering, University of Cambridge, UK.
[iii)] Professor of Civil Engineering, Waseda University.
[iv)] Chief cleak of Nishimatsu Research Institute, Nishimatsu Construction Co., LTD.
[v)] Reader in Engineering, University of Cambridge, UK.

Manuscript was received for review on November 11, 1998.
Written discussions on this paper should be submitted before January 1, 2000 to the Japanese Geotechnical Society, Sugayama Bldg. 4F, Kanda Awaji-cho 2-23, Chiyoda-ku, Tokyo 101-0063, Japan. Upon request the closing date may be extended one month.

istics of the machine and the construction process.

Because of the complex boundary conditions of a shield tunnelling problem, the use of the finite element method is one of the popular methods to investigate the ground deformation behaviour. In general, the finite element analysis results reported in the literature have contributed greatly in understanding various deformation mechanisms associated with shield tunnelling (e.g. Katzenbach and Breth, 1981; Clough and Leca, 1989; Swoboda et al., 1989; Lee et al., 1992; Ohtsu et al., 1993; Addenbrooke, 1996, 1997; Addenbrooke et al., 1997; and many others). However, these past studies are often made to examine the above-mentioned factors individually. Also, many of the reported analyses use the in-situ stress condition as the initial condition of the problem without any in-depth consideration of other factors affecting the change in the stress state of the soil. For example, both the steering problem and interface friction problems are expected to influence the soil conditions around the shield machine at the same time during its advancement and their effects cannot possibly be analysed separately. Therefore, there is a need to examine the combined effect of various aspects of shield tunnelling operations on ground deformation within one analysis.

The construction process of a shield operation is often modelled by applying external forces, introducing traction, or forcing displacements at the boundary nodes of a finite element mesh under a spatially fixed tunnel configuration. In these analyses, the advancement of the shield machine is not modelled. In reality, however, the stress-strain state of the soil changes continuously as the shield machine advances and then passes the spatial point of interest. In order to fully understand the deformation mechanism associated with shield tunnelling, the stress history (or stress path) caused by shield advancement needs to be investigated.

In this study, the advancement of a shield machine and excavation at the cutting face are modelled, so that the effect of these construction processes on ground deformation and stress-strain behaviour of the soil around the tunnel can be examined. In open cut excavation problems, the finite element method has proved to be useful for design purposes, even though the actual process of excavation is not modelled in an exact manner. Therefore, an attempt was made to model the cutting operation of shield tunnelling within the framework of the finite element method.

The excavation and advancement of a shield machine are modelled by (i) remeshing the finite elements at each time step, (ii) introducing the excavating elements of a fixed size in front of the shield machine elements, and (iii) applying external forces such as jacking forces behind the shield machine and slurry (or earth) pressures at the cutting face. By doing so, it is aimed to satisfy the continuity condition as well as the boundary conditions of the problem.

The proposed modelling techniques are used to simulate shield tunnelling construction project through clayey ground in Tokyo. The results from the three dimensional coupled soil-pore water analysis were compared to the actual field measurements in order to examine the stress-deformation behaviour of the soils caused by the shield tunnelling operation.

The modelling method described in this paper originates from the study by Akagi and Komiya (1993). In the present study, their method has been modified by implementing a more robust remeshing procedure for three dimensional finite element analysis of tunnel excavation. The accuracy of this new method is verified by performing one-dimensional consolidation analysis and comparing its result to the theoretical solution. A three dimensional finite element analysis of shield tunnelling in soft clayey deposits was carried out using the new method. The computed three dimensional settlement trough and the effective stress paths in the clay around a shield machine are carefully examined and reported in this study.

FINITE ELEMENT MODELLING OF EXCAVATION AND ADVANCEMENT OF A SHIELD MACHINE

EXCAVATING ELEMENT

In shield tunnelling work, the soil in front of the cutting face of a shield machine is extremely disturbed by its cutting operation. The exact operation of the cutting process is very difficult to model in the finite element method, because the excavation process itself violates the assumption of continuum mechanics used in the finite element formulation. In the past, this excavation process was commonly modelled by removing the finite elements in front of the machine and applying nodal forces at the boundary, which represents the cutting face (*see* Fig. 2). The applied nodal forces are obtained from the given (or recorded) hydraulic jack forces behind the machine and/or the earth/slurry pressures at the cutting face. Although this modelling technique satisfies the force boundary conditions, the sum of the computed nodal displacements at the cutting front and the length of the removed elements may not necessarily match the actual movement of the shield machine at a given time interval.

In this study, the excavation process is modelled by introducing new excavating finite elements of a fixed size in front of the shield machine (*see* Fig. 3). Solid finite elements are used for the excavating elements, and the presence of these elements in front of the cutting face aims to represent the disturbed area of the ground caused by the excavation process. Mathematically, the introduction of the excavating elements provides the condition where both displacement and force boundaries given by the shield machine operation are satisfied. The boundary conditions are (a) the known advancement of the machine at a given time interval, (b) the given (or recorded) external forces applied by the hydraulic jacks placed between the machine and tunnel lining, and (c) the given (or recorded) earth pressure or slurry pressure at the cutting face.

When various external forces are applied at the bound-

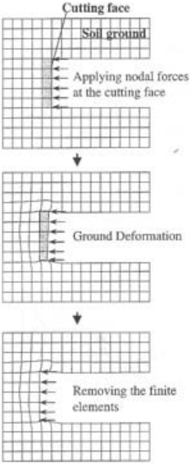

Fig. 2. Conventional excavation modelling

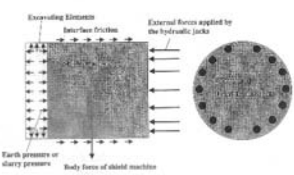

(a) Side view (b) Back view

Fig. 3. Excavation modelling using the excavating element

aries of the shield machine as shown in Fig. 3, the process of excavation is represented by the (artificial) deformation of the excavating elements. The size and the constitutive model used for the excavating element are rather arbitrary. However, they need to be selected so that the calculated movement of the shield machine controlled by the given force boundary conditions matches the recorded movement of the shield machine. In this study, the isotropic elastic model was used for convenience. In practice, the size and material properties of the excavating elements are determined by trial and error, so that the computed data are compatible with the monitoring data. However, the elastic properties of the excavating element should be mainly related to the characteristics of the shield machine (shape of the cutter, etc.) and the workmanship. The method which determines the material properties of the excavating elements will be described in detail later on.

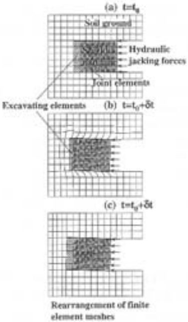

Fig. 4. Advance of shield machine simulated using excavating elements

MODELLING OF SHIELD MACHINE ADVANCEMENT

The advancement of a shield machine is modelled by (i) remeshing the finite elements at each time step, (ii) introducing the excavating elements of a fixed size in front of the shield machine elements, and (iii) applying external forces such as jacking forces behind the shield machine and slurry (or earth) pressures in front of the machine. Sequential illustrations of the finite element modelling of the excavation at the cutting face of the shield machine and the advancement of the tunnelling machine are shown in Fig. 4. The shaded area in the figure represents the proposed excavating element.

Figure 4(a) shows the status of the shield machine at reference time t_0. In order to model the hydraulic jacking forces applied to the shield machine, forces are applied at the nodes that represent the tail end of the shield machine. The applied nodal forces are given from the forces of the hydraulic jacks measured in the field at a given time. For the case of simulating slurry type shield tunnel operation, slurry and water pressures can be applied in the excavating elements, as shown in Fig. 3.

During the time interval of t_0 to $t_0+\delta t$, the excavating elements and the soil elements adjacent to the shield machine will deform by the jacking forces under undrained, partially drained conditions, or fully drained conditions, depending on the speed of the shield machine and the permeability of the ground. The shield machine itself will act as a rigid body since a large value of stiffness is used for the elements representing the shield machine.

After obtaining a solution for $t=t_0+\delta t$, the finite elements are remeshed as shown in Fig. 4(c). The new mesh will have the same mesh geometry relative to the shield machine as $t=t_0$, but the location of the shield has shifted. Again, the excavating elements will be placed in front of the cutting face before applying external forces given for the next time step. By doing so, the advancement of the shield machine and the associated stress-strain changes of the ground are numerically simulated in a continuous manner.

UPDATING EFFECTIVE STRESSES AND PORE PRESSURES IN REARRANGED MESH

After remeshing, the values of effective stresses and pore pressures of the remeshed elements need be calculated from those obtained in the original deformed mesh. This is necessary because the equilibrium condition needs to be satisfied before conducting the next loading step. The stress interpolation procedure is summarised in the flow-chart shown in Fig. 5.

STEP 1: Element Identification

The first step of the interpolation procedure is identifying an element, which has the rearranged nodal point inside it. The three dimensional finite element used in this study is the eight-noded trilinear element. Let a rearranged nodal point n_R exist inside an element that has eight nodes of n_1 to n_8, as shown in Fig. 6(a). In this case, the volume of the element should be equal to the volume sum of the quadrangular pyramids (V_1 to V_6 as shown in Fig. 6(b)), which are formed by the side plane of the element and the rearranged nodal point n_R. When nodal displacements are small, the volume of V_1 to V_6 can be evaluated by the following vector calculations.

$$\begin{aligned}
V_1&=(1/6)\{(\overrightarrow{n_1n_2}\times\overrightarrow{n_1n_3})+(\overrightarrow{n_1n_3}\times\overrightarrow{n_1n_4})\}\cdot\overrightarrow{n_1n_R}\\
V_2&=(1/6)\{(\overrightarrow{n_1n_5}\times\overrightarrow{n_1n_6})+(\overrightarrow{n_1n_6}\times\overrightarrow{n_1n_2})\}\cdot\overrightarrow{n_1n_R}\\
V_3&=(1/6)\{(\overrightarrow{n_2n_6}\times\overrightarrow{n_2n_7})+(\overrightarrow{n_2n_7}\times\overrightarrow{n_2n_3})\}\cdot\overrightarrow{n_2n_R}\\
V_4&=(1/6)\{(\overrightarrow{n_3n_7}\times\overrightarrow{n_3n_8})+(\overrightarrow{n_3n_8}\times\overrightarrow{n_3n_4})\}\cdot\overrightarrow{n_3n_R}\\
V_5&=(1/6)\{(\overrightarrow{n_4n_8}\times\overrightarrow{n_4n_5})+(\overrightarrow{n_4n_5}\times\overrightarrow{n_4n_1})\}\cdot\overrightarrow{n_4n_R}\\
V_6&=(1/6)\{(\overrightarrow{n_5n_6}\times\overrightarrow{n_5n_7})+(\overrightarrow{n_5n_7}\times\overrightarrow{n_7n_8})\}\cdot\overrightarrow{n_5n_R}
\end{aligned} \tag{1}$$

where × is the vector product and • is the scalor product.

If the rearranged nodal point exists outside the element, the volume sum of V_1 to V_6 will be larger than the element volume V. By doing this operation, the element, where the rearranged nodal point exists, can be identified automatically. This operation is performed for all the rearranged nodal points.

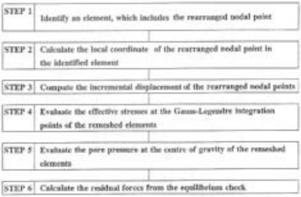

STEP 1 Identify an element, which includes the rearranged nodal point

STEP 2 Calculate the local coordinate of the rearranged nodal point in the identified element

STEP 3 Compute the incremental displacement of the rearranged nodal points

STEP 4 Evaluate the effective stresses at the Gauss-Legendre integration points of the remeshed elements

STEP 5 Evaluate the pore pressure at the centre of gravity of the remeshed elements

STEP 6 Calculate the residual forces from the equilibrium check

Fig. 5. Flow-chart of the stress interpolation procedure

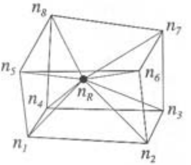

Fig. 6(a). Eight-noded trilinear element and a rearranged nodal poin n_R

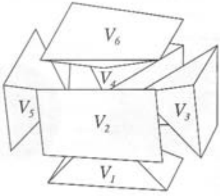

Fig. 6(b). The volume sum of the quadrangular pyramids

STEP 2: Local Coordinates Calculation

The local coordinate system of an eight-noded trilinea element is shown in Fig. 7. Assuming that the rearrange nodal point exists in an element, which has nodal poin n_1 to n_8, the local coordinate (ξ, η, ζ) of the rearrange nodal point is calculated using the flow chart shown i Fig. 8. The computational algorithm shown in the figur utilises Eq. (1) to save computing time. The operatio "*calc*" in the flow chart is described in Appendix A.

STEP 3: Incremental Displacement Vector Calculatio

The internal incremental displacement vector du_R a

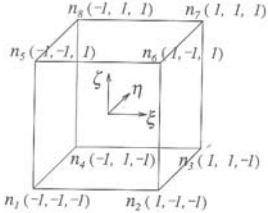

Fig. 7. Local coordinate system of eight noded trilinea element

the rearranged nodal point n_R can be computed from its local coordinate and the incremental displacement vectors of the nodal points n_1 to n_8, using the following equation

$$du_R = N_i(\xi, \eta, \zeta)du_i \tag{2}$$

where $N_i(\xi, \eta, \zeta)$ $(i=1, 8)$ is the shape function, and du_i is the incremental displacement vector at nodal point n_i of the element.

STEP 4: Effective Stress Update

Once the incremental displacement vector of all rearranged nodal points is computed, the effective stress increment $d\sigma'$ at the Gauss-Legendre integration points of the new remeshed finite elements are estimated using the following equation.

$$d\sigma' = \int \boldsymbol{D}\boldsymbol{B}du_R \tag{3}$$

where $\boldsymbol{D}$ is the stress-strain relationship of the soil skeleton at the Gauss-Legendre integration points, and $\boldsymbol{B}$ is the strain-displacement matrix. The selection of $\boldsymbol{D}$ depends on the state of the soil; so that correct stress path can be followed during the updating of the effective stresses. The effective stresses σ' at the Gauss-Legendre integration points of the remeshed elements at $t = t_0 + \delta t$ will be

$$\sigma' = \sigma_0' + d\sigma' \tag{4}$$

where σ_0' is the effective stress state at $t = t_0$. Ideally, σ_0' should be determined from the effective stress field at $t = t_0$ obtained in the original undeformed mesh. This requires back-calculating the location of the Gauss-Legendre integration points of the remeshed elements at $t = t_0$, and interpolating σ_0' at these points. However, this additional calculation increases the computing time. Therefore, in this study, σ_0' at the Gauss-Legendre integration point of the remeshed elements is simply assumed to be equal to that of the original undeformed element, provided that the incremental displacements computed at each time step are small. The details of the effective stress updating procedure used in this study are described in Appendix B.

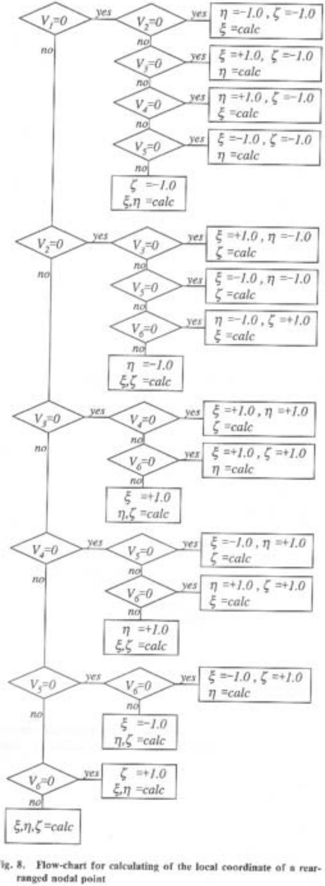

Fig. 8. Flow-chart for calculating of the local coordinate of a rearranged nodal point

STEP 5: Pore Pressure Update

In this study, the coupled stress-deformation-pore pressure interaction was formulated using the method proposed by Akai and Tamura (1978). This method is similar to the one proposed by Christian and Boehmer (1970), where the pore pressure is assigned at the centre of the element. When remeshing is performed, the value of pore water pressure in the element must be updated to satisfy the total stress equilibrium condition.

In this study, it is assumed that the total stresses of the remeshed element are equal to those of the original deformed element at $t=t_0+\delta t$. With this assumption, the pore water pressure p_{wR} of a remeshed element at $t+\delta t$ becomes the sum of the pore pressure of the deformed elements before remeshing and the change in the mean effective stress σ'_m of the remeshed element, as shown in the following equation.

$$p_{wR}=p_w+\sigma'_m-\sigma'_{mR} \tag{5}$$

where p_w is the pore water pressure before remeshing, σ'_m is the mean effective stress of the element before remeshing and σ'_{mR} is that after remeshing.

STEP 6: Residual Forces Calculation

The simplified evaluation of σ'_0 and $d\sigma$ used in Step 4 and 5 will produce some errors when equilibrium is checked. These errors result in residual forces. After stress updating, the residual forces of the rearranged nodal forces $d\phi_R$ are computed using the following equation.

$$d\phi_R=\int Bd\sigma_R dV-dF \tag{6}$$

where dF is the external incremental forces.

Further iteration of Step 4 and 5 can be made to obtain the correct stress/pore pressure field in the remeshed condition that satisfies the equilibrium condition. However, this iteration would result in a dramatic increase of computing time. Therefore, in this study, the residual forces computed at the rearranged nodal points are simply added to the loading forces of the subsequent incremental step. A similar technique is used in CRISP94 (Britto, 1994).

SIMULATION OF ONE-DIMENSIONAL CONSOLIDATION USING REMESHING TECHNIQUE

In order to verify the accuracy of the proposed remeshing technique, one-dimensional consolidation finite element analyses with and without the remeshing technique were performed, and the results were compared to Terzaghi's consolidation theory solution.

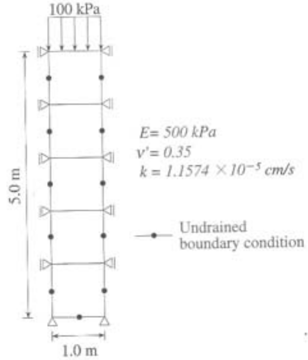

Fig. 9. Finite element model used in the one-dimensional consolidation problem

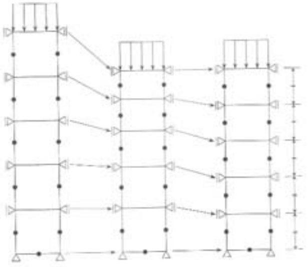

(a) $t=t_0$ (b) $t=t_0+\delta t$ (c) $t=t_0+\delta t$

Fig. 10. Rearrangement of finite element meshes

The finite element meshes and the material properties used in these analyses are shown in Fig. 9. After obtaining a solution for $t=t_0+\delta t$ (Fig. 10(b)), the finite elements were remeshed as shown in Fig. 10(c) and the stress state of each remeshed element was updated. All the remeshed elements have the same mesh geometry. The results of the analyses are compared to Terzaghi's consolidation solution for the relationship between the time factor T_v and the degree of consolidation U which is defined as the percentage of the current surface settlement to the final surface settlement, as shown in Fig. 11. The solid circles in the figure are the results obtained by the remeshing technique, whereas the open circles are the results obtained without the remeshing technique. The numerical analysis with the remeshing technique appears to give a better match to Terzaghi's solution.

The computed isochrone curves of the excess pore water pressure are shown in Fig. 12(a) for analysis with remeshing and (b) for analysis without remeshing. The vertical axis of the figures is the ratio of the distance from the drained surface z to the initial height of the model z_0, whereas the horizontal axis is loaded pressure p (=100 kPa). The result of the analysis with remeshing provides a better match to the theoretical solution, especially at the beginning of the consolidation and at locations close to the drainage boundary.

THREE DIMENSIONAL FINITE ELEMENT MODELLING OF SHIELD TUNNELLING

During shield tunnelling work, the position and direction of the shield machine are controlled by changing the driving forces of the hydraulic jacks installed behind the machine. Therefore, three dimensional movements of the machine, i.e. the pitching and yawing, take place in a complicated manner.

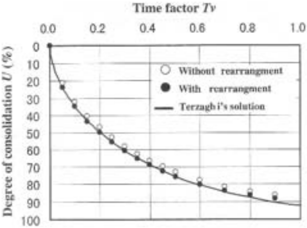

Fig. 11. Relations between the degree of consolidation U and time factor-T_v

Complicated boundary conditions exist, particularly in the case of shield tunnelling in urban areas, since the distance between the shield tunnel and the pre-existing underground structures or the foundations of superstructures frequently becomes very small. Hence, the three dimensional nature of a shield tunnelling problem must be considered carefully in order to have proper control of the construction.

The long term subsidence around a tunnel is directly related to the excess pore pressures generated during the shield machine advancement. Therefore, the coupled soil-pore water analysis is necessary to assess the time-dependent ground deformation caused by shield tunnelling construction.

With the above considerations in mind, a three dimensional coupled soil-pore water analysis was conducted to simulate the construction process of a tunnel of 3.7 m diameter in Tokyo. The tunnel was approximately 33 m deep, and 0.55 km long. The machine used was of shield type with an earth pressure balance, and air bubbles were injected in the excavation chamber to stabilise the soil and control the earth pressure in front of the shield machine.

FINITE ELEMENT MODELLING

Soil Modelling

The Sekiguchi and Ohta's model (1979) was used to model the stress-strain behaviour of the clay. The input parameters used in the analysis are listed in Table 1. Most of the input parameters were determined from the results provided by standard geotechnical tests on samples obtained at various depths. Other input parameters, which were not able to be determined from these tests, were calculated by the method suggested by Iizuka et al. (1985).

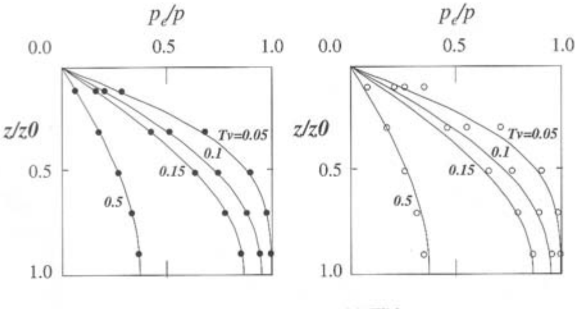

(a) With rearrangement (b) Without rearrangement

Fig. 12. Isochrone curves of excess pore water pressure

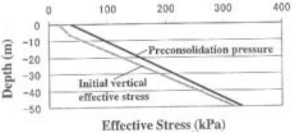

Fig. 13. Preconsolidation pressure and initial vertical effective stress

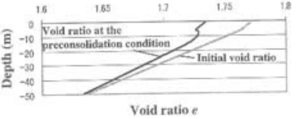

Fig. 14. Distribution of void ratio with depth

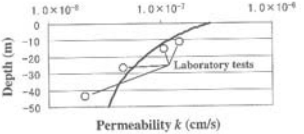

Fig. 15. Distribution of permeability with depth

The initial distribution of the preconsolidation pressure was obtained based on the results of standard oedometer consolidation tests. The variation of preconsolidation pressure versus depth used for the analysis is shown in Fig. 13.

The initial distribution of the water content was obtained from the samples taken, and the unit weight of the soil was estimated by assuming that the soil is fully saturated. The initial void ratio distribution is shown in Fig. 14. The ground water table was assumed to be at the ground surface and initially hydrostatic water condition. Accordingly, the initial vertical effective stresses were computed as shown in Fig. 13. The coefficient of lateral earth pressure was assumed to be 0.55, irrespective of the overconsolidation ratio.

The coefficient of permeability at various depths was estimated by the method proposed by Iizuka et al. (1985), which uses the preconsolidation pressure and the void ratio at the preconsolidation pressure. The distribution of the coefficient of vertical permeability is shown in Fig. 15. For comparison, the values measured from the oedometer tests are plotted in the figure. The measured values (as shown in white circle symbols in the figure) agree well with the estimated profile.

Values of coefficient of horizontal permeability were not measured in the laboratory. They were assumed to be twenty times those of vertical permeability, as it is common that the horizontal permeability is larger than the vertical.

Shield Machine Modelling

The shield machine was modelled as a rigid body by assigning a large value of elastic modulus of 2.0×10^8 (kN/m^2) and Poisson's ratio of 0.499. The weight of the machine was modelled by applying a body force. The diameter and length of the shield machine are 3.737 m and 5.67 m, respectively.

Shield Machine and Soil Interface Modelling

It has been recognized that the long-term subsidence after soft clay tunnelling is partly caused by excess pore pressure induced by disturbance associated with the interface friction between the soil and shield machine. Therefore, joint elements were placed at the interface of the elements that represent the shield machine and the adjacent soil, in order to investigate interface friction effects on ground deformations. The behaviour of the joint elements shows zero stiffness when the frictional force exceeds some critical value.

Table 1. Input parameters for shield tunnelling simulation

Shield machine	Young's modulus E Poisson's ratio ν Density ρ	1.96×10^8 kPa 0.499 3.00 g/cm^3
Excavating element	Young's modulus E Poisson's ratio ν Density ρ	138.3 kPa 0.100 1.62 g/cm^3
Cohesive soil	Specific gravity of soil particle Gs Compression index λ Swelling index κ Poisson's ratio ν Critical state parameter M Density of saturated soil ρ_{sat}	2.680 0.320 0.054 0.355 1.05 1.62 g/cm^3
Joint element	Yield value τ_y	4.9 kPa

Excavating Elements

The excavating elements represent the area that is disturbed by cutting and mixing of the excavated soils with slurry in front of the cutting face of the shield machine. The excavating elements are used to match the volume change and shear distortion of the elements to the actual movement of the shield machine. Therefore, the material properties of the excavating elements depend on various factors such as the method of excavation, machine characteristics, the size of the elements, etc. Hence, they need to be obtained by trial and error.

In this analysis, the excavating element was assumed to be an isotropic elastic material, and the thickness of the excavating elements was selected to be 20 cm. The air bubble pressure measured during the construction was applied as a pressure boundary within the excavating elements. The measured jacking forces were applied as nodal forces behind the shield machine. The elastic properties of the excavating elements were then determined by matching the computed advancement of the shield machine at a given time step to the measured field movement data. The initial analysis showed that a Young's modulus of 141 kPa and Poisson's ratio of 0.1 should be used in the subsequent machine advancement analysis.

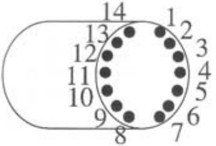

Fig. 16(a). Location of fourteen hydraulic jacks

Shield Machine Operation

The advancement of the shield machine was simulated by applying forces at the tail of the shield machine, where the hydraulic jacks are located, and providing pressures inside the excavating elements. The applied forces and pressures were obtained from the actual driving records of the machine. In this construction, fourteen hydraulic jacks were installed behind the machine as shown in Fig. 16(a). The jacking records are shown in Fig. 16(b), where the top column is the elapsed time. In this shield operation, each hydraulic jack did not operate independently, and the jacks were in the mode of either on or off. The solid circles in the bottom column of Fig. 16(b) show the time sequence of on/off mode of each hydraulic jack. The values in the central row of Fig. 16(b) are the combined hydraulic force of all the jacks in operation. Hence, the driving force of each jack can be computed by dividing this combined hydraulic force by the number of jacks in operation.

After the tunnel linings are installed, ground movement occurs as the earth pressure is released in the tail void, which corresponds to the space made between the excavated area of the tunnel machine and the outer surface of the tunnel lining. In order to avoid this ground movement, backfill injection is commonly made into the tail void. In this analysis, the finite element meshes adjacent to the tunnel lining were expanded in a radial direction by applying a pressure equivalent to the measured backfill pressure. Once the backfill operation was completed, the nodal displacements were fixed in position.

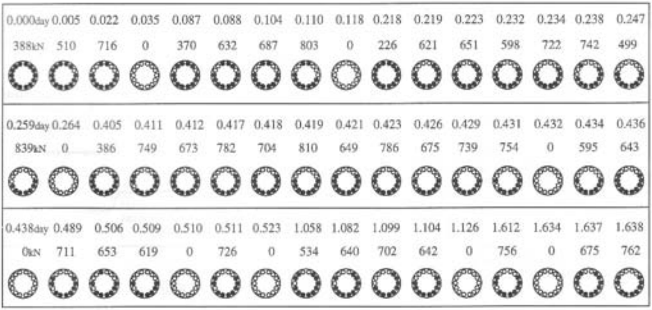

Fig. 16(b). The jacking record

NUMERICAL RESULTS

Ground Settlements

The three dimensional views of the computed settlement trough at 1 m above the crown of the machine at various times are shown in Fig. 17. The sequence of finite element remeshing operation with the machine advancement is illustrated in the figure.

In this case study, the subsurface displacements and pore water pressures were also measured at 1 m above the crown of the shield machine as the machine passed the measurement point. The arrow in Fig. 17 shows the measurement point. The surface settlement was also measured.

The computed vertical displacements at the ground surface and at 1 m above the crown are shown in Fig. 18. The horizontal axis of the figure is the elapsed time from the beginning of the numerical simulation. The measured data are also plotted in the figure for comparison. Although the measured data show that there is a sudden ground upheaval approximately 10 hours after the arrival of the shield machine face due to some unknown reason, both the calculated and measured vertical displacements are almost identical after the passage of the tail of the shield machine. The vertical settlement after the shield machine passed the measurement point was 6.9 mm, which corresponds to the measured displacement in the field. The vertical ground surface displacement was almost zero in this case. It is important to notice here that the field monitoring was stopped when the tail of the machine passed the measuring point. Therefore, the deformation related to tail void closure is not modelled in this analysis, and larger vertical displacement is expected to occur in the later stage of tunnel construction.

The contour plot of the vertical displacements at 1 m above the crown at $t=1.64$ days is shown in Fig. 19. Due to variation in the jacked forces applied to the machine, there was an upheaval of approximately 8 mm in front of the machine. Unfortunately, the field measurement started just before the machine approached to the monitoring point. Therefore, it was not possible to compare this computed result to the actual upheaval behaviour in the field.

Peck (1969) showed that the transverse surface settlement trough immediately following tunnel construction is well-described by the following Gaussian distribution curve.

$$S_v = S_{\max} \cdot \exp\left(-y^2/2i^2\right) \tag{7}$$

where S_v is the vertical settlement, $S_{\max}$ is the maximum settlement on the tunnel centre line, y is the horizontal distance from the tunnel centre line and i is the horizontal distance from the tunnel centre line to the point of inflexion of the settlement trough. The computed settlement trough at 1 m above the crown of the tunnel lining was fitted by the Peck's Gaussian distribution curve, as shown in Fig. 20. The maximum settlement at the centre of the tunnel was 6.9 mm. The shape of the computed settlement trough at 1 m above the crown of the shield tail is similar to the one suggested by Peck.

Pitching Angle of the Shield Machine

The computed vertical tilt of the shield machine, i.e. the pitching angle θ, is plotted against the elapsed time in Fig. 21. The recorded pitching angle of the machine is also plotted in the figure.

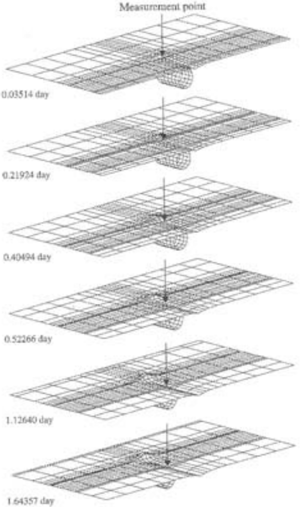

Fig. 17. Three dimensional views of the computed settlement (1 m above the crown of the machine)

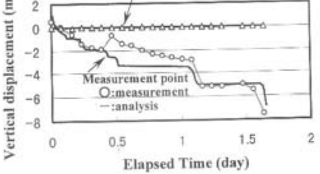

Fig. 18. Vertical displacement at the ground surface and at 1 m above the crown

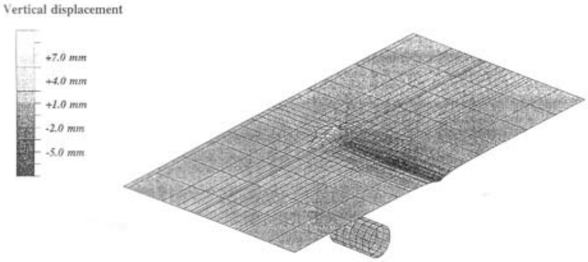

Fig. 19. Contour plot of the vertical displacements (1 m above the crown, $t = 1.64$ day)

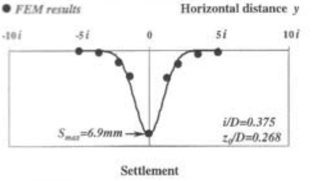

Fig. 20. Gaussian curve used to describe the transverse settlement trough

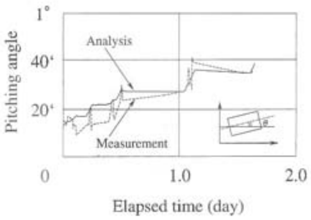

Fig. 21. Pitching angle of the shield machine

The figure shows that the pitching angle increased suddenly when the machine started to operate, implying that the machine was inclined from the horizontal level. The angle increased as the machine advanced and the increase ceased when the machine stopped. This is mainly due to the variation in the mechanical jacking forces applied behind the machine, which is controlled by the machine operator. This is one of the reasons that some upheaval ground movement was observed in front of the machine.

During the advancement, the upper tail of the machine is moving away from the tunnel linings as it excavates, providing a larger tail void space at the crown of the tunnel. On the other hand, at the invert section, the lower tail of the shield should be providing a downward force to the ground.

Stress Paths of the Soil Around the Shield Machine

The effective stress paths in the soft clay around the shield machine during the advancement are shown in Fig. 22. The stress paths are plotted in terms of mean effective stress p' and deviator stress $q = \sqrt{2J_2}$, where J_2 is the second invariant of the deviator stress tensor. Eight elements adjacent to the circumferential face of the shield machine were selected for plotting. The initial K_0 line, the critical state line and the current yield surface based on the Sekiguchi-Ohta model are also drawn in the stress path figures.

The results show that the elements around the crown of the machine (solid circles in the figure) are in a condition of unloading due to stress release as the machine passes along the element. The effective stress states move within the current yield surface, producing some elastic unloading deformation.

The positive pitching angle of the machine shown in Fig. 21 suggests that the lower tail of the shield is providing a downward force to the ground. The elements below the invert of the machine (open circles in the figure) are in the condition of loading due to the weight of the machine and the jacking operation. In this area, the yield surface of the soil expands from its initial condition, producing some plastic strains.

Excess Pore Pressure Generation

The calculated and measured excess pore water pressure changes at the measuring point above the crown of

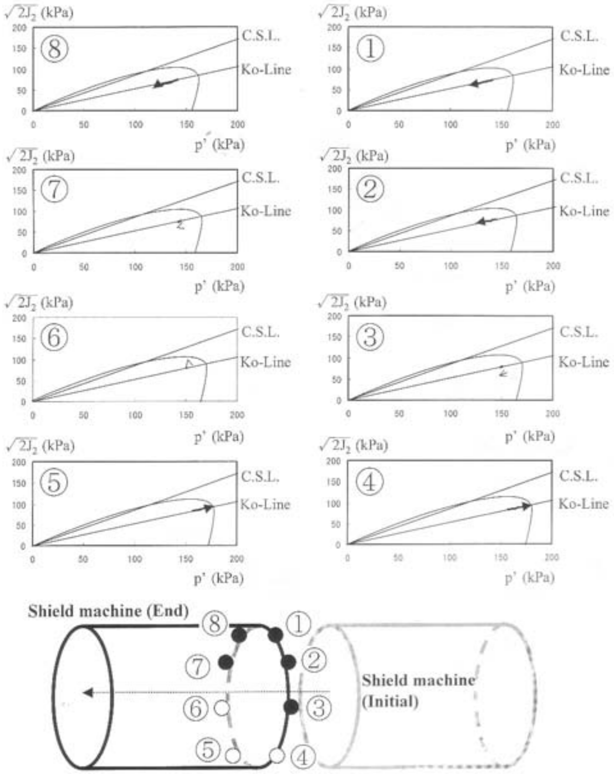

Fig. 22. Stress paths of the soil around the shield machine

the shield machine are shown in Fig. 23. The initial increase in excess pore pressure is due to stress created at the face by the jacking force. The finite element result shows that the excess pore pressures become negative as the shield machine passes the measurement point. This is due to the unloading of the soil, as illustrated in Fig. 22. The measured value, however, demonstrated a sudden increase in excess pore water pressure approximately 10 hours from the arrival of the shield machine for some unknown reason. Such a discrepancy between the measured and calculated values is similar to the sudden change in measured vertical settlement shown in Fig. 18.

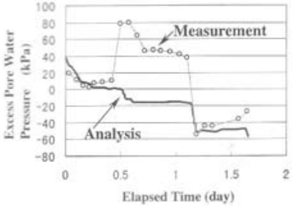

Fig. 23. Variation of excess pore water pressure at 1 m above crown

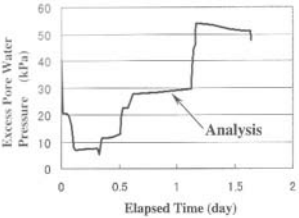

Fig. 24. Variation of excess pore water pressure at the bottom of the shield machine

The calculated excess pore water pressure at the bottom area of the shield machine is shown in Fig. 24. Again, there is an initial increase in excess pore pressure when the point of interest is in front of the machine. As the machine passes, there is an increase in excess pore pressure due to the loading condition observed at this location.

The results shown in Figs. 23 and 24 imply that the pore water pressure behaviour during shield tunnelling is closely related to loading/unloading condition of the soil caused by the positional and directional change of the shield machine. The pattern and magnitude of the excess pore pressures generated during the shield machine advancement will directly affect the long term subsidence around the tunnel, especially in the case of shield tunnelling through soft ground. Therefore, the postural change of the shield machine needs to be modelled, and controlled as accurately as possible for assessing the short and long term ground settlement due to shield tunnelling construction.

CONCLUSIONS

In this paper, the advancement and excavation processes of shield tunnelling operations were modelled using the finite element method in order to investigate the effect of these construction processes on the ground response. A new excavating finite element, which modells the disturbed soil in front of the cutting face, was proposed. The operation of shield advancement and of soil excavation was simulated using the finite element remeshing technique at each time step of the analysis.

The proposed modelling techniques of shield tunnelling construction were applied to simulate tunnelling project in soft cohesive soil in Tokyo and the results were compared with the field measurements. The soil deformation mechanism associated with the shield tunnelling operation was examined in detail. The vertical ground displacement profile, the effective stress paths in the soft clay, the excess pore water pressures, and the postural change of the shield machine, were obtained from the three-dimensional finite element simulation using the proposed modelling technique, and the results agreed with the field observations.

The cohesive soil around the crown of the machine was in a condition of unloading, due to the stress release as the machine passes. The effective stress states moved within the current yield surface, producing some elastic unloading deformation. The excess pore pressure became negative around the crown as the shield machine passes.

At the invert section, on the other hand, the lower tail of the shield was providing a downward force to the ground. The ground in this region was in a condition of loading due to the weight of the machine and the jacking operation. Therefore, the yield surface of the soil expanded from its initial condition producing some plastic strains. The excess pore pressures increased due to the loading condition at this location.

These pore pressures provide its proper input to a long-term analysis of the loading on the tunnel lining, and of ground surface displacements.

ACKNOWLEDGEMENT

The financial support of this research was provided by European Commission under the Brite Euram III program. Their support is gratefully acknowledged.

REFERENCES

1) Addenbrooke, T. I. (1996): "Numerical analysis of tunnelling in stiff clay," PhD thesis, Imperial College of Science Technology and Medicine.

2) Addenbrooke, T. I., Potts, D. M. and Puzrin, A. M. (1997): "The influence of pre-failure soil stiffness on the numerical analysis of tunnel construction," Géotechnique, Vol. 47, No. 3, pp. 693-712.

3) Akai, K. and Tamura, T. (1978): "Numerical simulations of multi-dimensional consolidation caused by elasto-plastic constitutive equation," J. of Geotech. Engrg., No. 269, Japanese Society of Civil Engineers, pp. 95-104 (in Japanese).

4) Akagi, H. and Komiya, K. (1993): "Finite element analyses of the stress–deformation behaviour considering the execution procedures during shield work," J. of Japan Society of Civil Engineers, No. 483/III-25, pp. 59-68 (in Japanese).

5) Britto, A. M. (1994): CRISP 94, User's and Programmer's Guide,

Cambridge University Engineering Department.
6) Christian, J. T. and Boehmer, J. W. (1970): "Plane strain consolidation by finite elements," J. of Soil Mech. Found. Div., ASCE, Vol. 94, No. SM4, pp. 1435–1457.
7) Clough, G. W. and Leca, E. (1989): "With focus on use of finite element methods for soft ground tunnelling," Review paper in Tunnels et Micro-Tunnels en Terrain Meuble-du Chantier a la Theorie, Presse de l'Ecole Natinale des Ponts et Chaussees, Paris, pp. 531–573.
8) Hashimoto, S. (1984): "Results of shield tunnelling in vertical close to existing shield tunnels," J. of Geotech. Engrg., No. 352, III-2, Japanese Society of Civil Engineers, pp. 1–22 (in Japanese).
9) Iizuka, A., Ohta, H. and Yoshimine, T. (1985): "Input parameters of the elast-visco-plastic finite element method," Proc. of 20th Annual Meetings on Japanese Society on Soil Mechanics and Foundation Engineering, pp. 973–974 (in Japanese).
10) Katzenbach, R. and Breth, H. (1981): "Nonlinear 3D analysis for NATM in Frankfurt Clay," Proc. 10th Int. Conf. on SMFE, Stockholm, Vol. 1, pp. 315–318.
11) Lee, K. M., Rowe, R. K. and Lo, L. Y. (1992): "Subsidence owing to tunnelling. I. Estimating the gap parameter," Can. Geotech. J., Vol. 29, pp. 929–940.
12) Mair, R. J. and Taylor, R. N. (1997): "Bored tunnelling in the urban environment," Theme lecture to 14th Int. Conf. on SMFE, Hamburg, Vol. 4.
13) Ohta, H. and Sekiguchi, H. (1979): "Constitutive equations considering anisotropy and stress reorientation in clay," Proc. of 3rd Int. Conf. on Numerical Method in Geomechanics, Aachen, Vol. 1, pp. 475–484.
14) Ohtsu, H., Ohnishi, Y., Taki, H. and Kamemura, K. (1993): "A study on problems of excavation analysis based on the concept of effective stress," J. of Geotech. Engrg., No. 481, III-25, Japanese Society of Civil Engineers, p. 77–85 (in Japanese).
15) Owen, D. R. J. and Hinton, E. (1980): Finite Elements in Plasticity, Pineridge Press Limited, UK, Chapter 8.
16) Peck, R. B. (1969): "Deep excavations and tunnelling in soft ground," Proc. 7th Int. Conf. on SMFE, Mexico City, State of the Art Volume, pp. 225–290.
17) Swoboda, G., Mertz, W. and Schmid, A. (1989): "Three dimensional numerical models to simulate tunnel excavation," NUMOG III, Pande. Elsevier Science Publishers Ltd., London, pp. 536–548.

NOTATION

$\cdot$ = Scaler product
$\times$ = Vector product
B = Strain-displacement matrix
D = Diameter of shield machine
D = Stress-strain matrix
F = External force
J^{-1} = Jacobin matrix inverse
J_2 = Second invariant of the deviator stress tensor
n_i = Nodal points of finite element
n_R = Remeshed nodal point
N_i = Shape function
p_w = Pore water pressure
p' or σ'_m = Mean effective stress
q = Deviator stress
$_R$[illegible] = After remeshing
S_v = Vertical settlement
u_i = Displacement vectors at the nodal points n_i
u_R = Displacement vectors at the remeshed nodal point n_R
ξ, η, ζ = Local coordinate of the iso-parametric finite element
ϕ = Residual forces of nodal forces

Appendix A

As shown in Fig. A-1, the mapping of vector dx within the finite element in the global coordinate system (x, y, z) to the vector dr with the local coordinate system of the element (ξ, η, ζ) is given by the following equation;

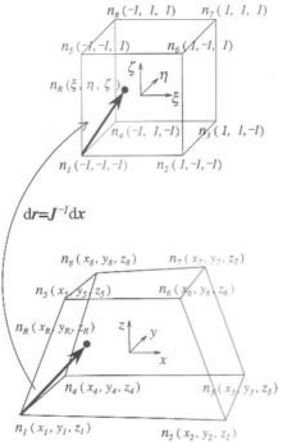

Fig. A-1. Mapping between the grobal and the local coordinate system

$$dr = J^{-1}dx \tag{A1}$$

where J^{-1} is the inverse of the Jacobin matrix.

The local coordinates of the rearranged nodal point n_R can then be found from the coordinate of one nodal point. For example using the nodal coordinate of n_1.

$$(\xi_R, \eta_R, \zeta_R) = J^{-1}(x_R - x_1, y_R - y_1, z_R - z_1) + (-1, -1, -1) \tag{A2}$$

where (ξ_R, η_R, ζ_R) is the local coordinates of the rearranged nodal point, (x_R, y_R, z_R) is the global coordinate of the rearranged nodal point, (x_1, y_1, z_1) is the global coordinates of the nodal point n_1 and $(-1, -1, -1)$ is the local coordinates of the nodal point n_1.

Appendix B

The effective stress state σ'_R at the Gauss-Legendre integration points of the remeshed elements at $t = t_0 + \delta t$ is computed using the following equation.

$$\sigma'_R = \sigma'_0 + d\sigma' \tag{B1}$$

where σ'_0 is the effective stresses estimated from the original undeformed mesh at $t = t_0$, $d\sigma'_R$ is the effective stress increment produced within a time step δt.

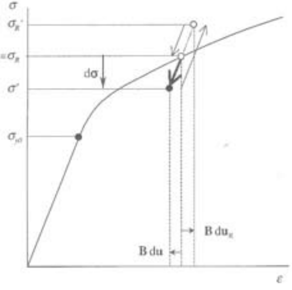

Fig. B-5.

step.

$$\sigma_R' = \sigma_0' + D_e d\varepsilon_R \tag{B2}$$

where D_e is the elastic stiffness.

Case 2 The new stress state of the original element is in the elastic region, whereas that of the remeshed element is in the plastic region (Fig. B-3)

In this case, the stress state calculated from Eq. (B2) will be outside the current yield surface for the remeshed element and the strain integration is necessary to compute the stress state σ_R' of the remeshed element. To reduce the computing time, σ_R' is simply corrected back to the yield stress state of the current yield surface using the method proposed by Owen and Hinton (1980).

Case 3 The stress state of both the original and remeshed element are in plastic condition (Fig. B-4)

Since both increments produce plastic deformation, the strain integration is necessary to obtain the stress state σ_R' of the remeshed element. In this case, σ_R' is assumed to be equal to the stress state of the original element σ'.

Case 4 The stress states of both the original and remeshed element are unloaded into the elastic region

Similar to Case 1, σ_R' is calculated to be equal to $\sigma_0' + D_e d\varepsilon_R$, where D_e is the elastic stiffness.

Case 5 The stress state of the original element becomes one of unloading, whereas that of the remeshed becomes one of plastic loading (Fig. B-5)

The stress state σ_R' is assumed to be equal to σ_0.